Journal of Power Sources 183 (2008) 388–398

Contents lists available at ScienceDirect

Journal of Power Sources

journal homepage: www.elsevier.com/locate/jpowsour

Thermally activated ("thermal") battery technology Part IV. Anode materials

Ronald A. Guidotti [a,*], Patrick J. Masset [b]

[a] Sierra Nevada Consulting, 1536 W. High Pointe Ct., –>Minden–>, –>NV–> 89423, –>United States–>
[b] Karl Winnacker Institut der DECHEMA e.V., Theodor-Heuss-Allee 25, 60486 Frankurt am Main, –>Germany–>

ARTICLE INFO

Article history:
Received 2 March 2008
Accepted 25 April 2008
Available online 14 May 2008

Keywords:
Thermal batteries
Thermally activated batteries
Molten salts
Anodes

ABSTRACT

In this paper, the history of anode materials developed for use in thermally activated ("thermal") batteries is presented. The chemistries (phases) and electrochemical characteristics (discharge mechanisms) of these materials are described, along with general thermodynamic properties, where available. This paper is the last of a five-part series that presents a general review of thermal-battery technology.

1. Introduction

We have reported on the history, development, and technology of thermally activated ("thermal") battery technology in earlier papers. The first paper dealt with a general overview [1], the second paper covered electrolytes [2], and the third and fourth papers dealt with cathode materials [3,4]. In this final paper of the series, we discuss anode materials.

2. Early technology

2.1. Ca and Mg anodes with WO_3 and V_2O_5 cathodes

The earlier technologies used Ca and Mg sheet (foil) anodes with WO_3 or V_2O_5 cathodes and LiCl–KCl eutectic electrolyte for fuzing application [5]. In the absence of displacement reactions with the electrolyte, these anodes would be expected to provide two equivalents per gram-atom of anode. The exact nature of the electrochemistry of these systems was not investigated in any detail but was used empirically by the thermal-battery design engineers, many of whom had little or no electrochemical background. Work was published by Laitenen et al., however, on the basic electrochemistry of V_2O_5 in molten salts [6,7]. It shows a multitude of oxidation states, leading to a series of voltage plateaus. (The high solubility of V_2O_5 – more than 17 w/o – complicated its use in thermal batteries, as it can lead to chloride oxidation in the melt.) Similar research efforts were never reported in the open literature for WO_3, however. This technology used glass tape impregnated with electrolyte for the separator.

2.2. Ca/$CaCrO_4$ couple

These earlier technologies were replaced by the Ca/$CaCrO_4$ system in the mid-1950s. From the early 1960s until into the 1970s, this couple (with an emf of over 3 V) was the primary technology for thermal batteries. (The $CaCrO_4$ replaced K_2CrO_4 that had been used earlier.)

2.2.1. Anode reactions

Since there is no separator present in the Ca/$CaCrO_4$ battery as it is constructed, the Ca anode is in direct physical contact with the $CaCrO_4$ cathode material that is dissolved in the LiCl–KCl eutectic melt (soluble to 34 w/o at 600 °C). Once the battery becomes activated, a chemical displacement reaction between Ca and the Li^+ present in the molten salt occurs, as shown in

$$2Ca + 2Li^+ \rightarrow CaLi_{2(liq)} + Ca^{2+} \quad (1)$$

Thus, a liquid Ca–Li alloy is the actual anode and not elemental Ca. This likely occurred with the earlier electrochemical systems using Ca and the LiCl–KCl eutectic. Since the anode is liquid, intercell shorting can occur if the alloy is not contained. The current collectors for the anode were undercut (smaller in diameter than the Ca) for this reason. The $CaLi_2$ discharges through several stages: $CaLi_2 \rightarrow CaLi \rightarrow Ca$. The Ca then reacts with the bulk Li^+ again (Eq.

* Corresponding author. Tel.: +1 775 267 1523; fax: +1 775 267 1523.
E-mail address: RonGuidotti@SierraNevadaConsulting.com (R.A. Guidotti).

0378-7753/$ – see front matter © 2008 Elsevier B.V. All rights reserved.
doi:10.1016/j.jpowsour.2008.04.090

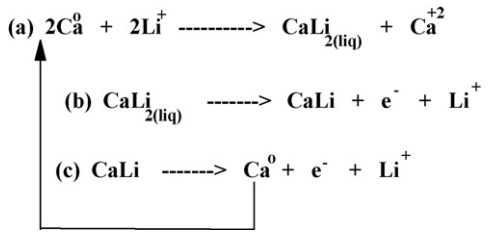

Fig. 1. Discharge reactions of Ca anode in $Ca/CaCrO_4$ thermal batteries.

(1)) to regenerate the $CaLi_2$ alloy anode. This is shown schematically in Fig. 1.

There is also the possibility of the Ca^{2+} participating in double-salt formation in the presence of K^+, as shown in

$$Ca^{2+} + K^+ + 3Cl^- \rightarrow KCaCl_{3(sol)} \quad (2)$$

The high melting point of the $KCaCl_3$ of 752 °C can cause salt precipitation at the anode–separator interface, increasing the cell impedance [8].

At the same time, the $CaLi_2$ that forms immediately reacts with the dissolved chromate to form a dark green Cr(V) compound that serves as the separator for the battery [9]. This is shown in

$$3CaLi_{2(liq)} + 4Cl^- + 17Ca^{2+} + 12CrO_4{}^{-2} \rightarrow 4Ca_5(CrO_4)_3Cl_{(s)} + 6Li^+ \quad (3)$$

Thus, both chemical as well as electrochemical reactions occur during discharge of such batteries. The chemical reactions must be controlled during discharge as they are exothermic and cause the battery to heat. Uncontrolled, they can lead to a thermal runaway where the battery destroys itself. Maintaining this delicate balance made the design of $Ca/CaCrO_4$ thermal batteries challenging.

3. Later technology

At the height of the use of the $Ca/CaCrO_4$ technology, little was known of the chemistry and materials properties that impacted performance. This resulted in much of the battery design being done empirically or based on previous experience. Later, the use of FeS_2 (pyrite) cathodes was introduced. This greatly simplified battery design because there were no major chemical reactions taking place between the electroactive components as in the $Ca/CaCrO_4$ system. In addition, the discharge mechanisms were well defined as a result of extensive work done at Argonne National Laboratory (ANL) for high-temperature, secondary applications.

3.1. Ca and Ca-alloy anodes

Some early work at ANL involved the use of Ca anodes with FeS_2 cathodes for use in high-temperature secondary batteries using $LiCl–NaCl–CaCl_2–BaCl_2$ electrolyte (m.p. = 383 °C) [10,11]. The work was extended to include Ca–Al, Ca–Si, Ca–Si, and mixtures of CaSi and $CaAl_2$, as well. The utilization of the Ca–Al–Si anodes was much greater than that of the Ca–Si anode. During recharge, the Ca_2Si that forms degraded the BN-felt separator that was used with Ca–Si anodes [12]. Ca anodes were also examined initially with FeS_2 cathodes at Catalyst Research Corp. (CRC) in the early 1970s but were dropped in favor of Li-alloy ones [13]. The major disadvantage of Ca anodes is the displacement reactions in the presence of Li^+ to form a liquid anode. The cell emf with Ca anodes is much less than that of Li-alloy anodes.

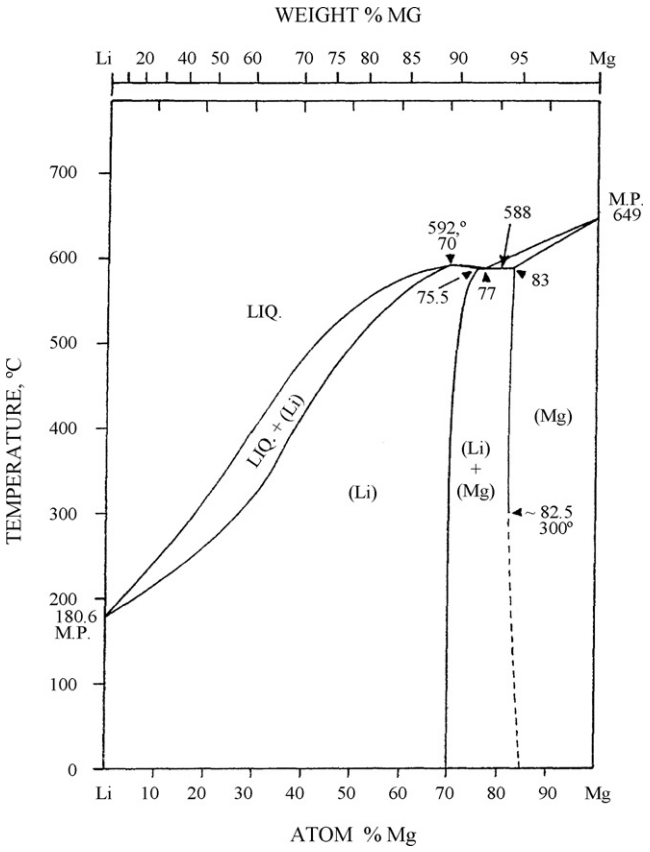

Fig. 2. Phase diagram of Li–Mg system.

3.2. Mg-based anodes

Work was done initially with the $Mg/LiCl–KCl/FeS_2$ system in the 1970s to demonstrate that this technology was much better than the older $Ca/CaCrO_4$ technology [14]. The use of Mg_2Si anodes containing Ca was examined at ANL for high-temperature rechargeable applications. During charging in $LiCl–KCl–CaCl_2$ electrolyte (m.p. = 350 °C), the Mg_2Si becomes a mixture of Ca–Mg–Si phases of composition $Ca_{1.5}Mg_2Si$ [15]. Problems were encountered with pure Mg, so Mg alloys such as Mg_2Al_3 and Mg_2Cu were also explored. The sluggish kinetics and lower emfs and capacities relative to the Li-alloy anodes resulted in only a limited development effort.

Mg–Si and Mg–B anodes have been reported to be rechargeable in molten-salt, high-temperature cells [16]. For this application, $MgCl_2$-containing electrolytes were used (e.g., $MgCl_2–NaCl$). However, no performance data were given.

The use of Li–Mg alloys was examined for use in high-temperature batteries. The Li–Mg phase diagram is shown in Fig. 2. The emfs of Li–Mg alloys was examined over a range of temperatures and composition in molten LiCl–KCl eutectic with the results presented in Fig. 3 [17]. No actual discharge tests were carried out with the alloys.

The diffusion coefficients in Li–Mg alloys were measured by Iwadate et al. at 420 °C by both galvanostatic and potentiostatic methods in LiCl–KCl eutectic [18]. Values for the α phase ranged from 3 to 9×10^{-10} cm^2 s^{-1}. Li diffusion was much faster in the β phase, being of the order of $\sim 10^{-6}$ cm^2 s^{-1}.

If such alloys are to be considered for use as anodes in high-temperature batteries, the mechanical processing becomes important. With that objective in mind, Sahoo and Atkinson stud-

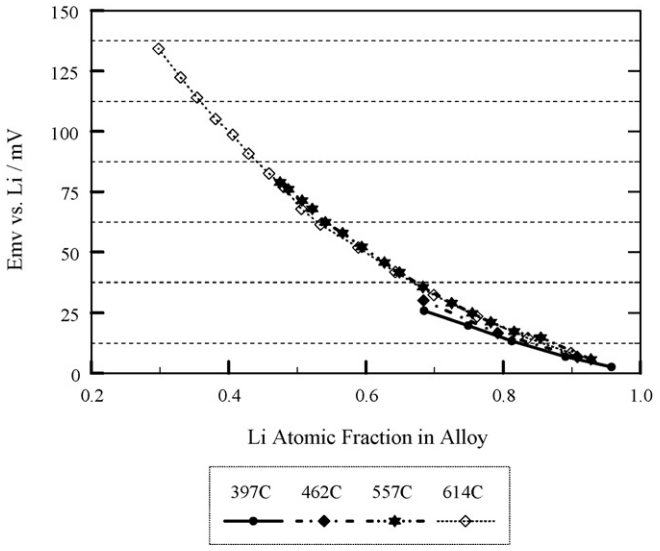

Fig. 3. Emf of molten Li–Mg alloys over a range of compositions and temperatures.

ied the fabrication of Li–Mg and Li–Mg–Al alloys [19]. The preferred approach was induction melting followed by annealing for single-phase alloys.

The thermodynamics and re-examination of the phase diagram were reported by Gasior et al. [20]. More recently, the mechanism of Li insertion into Li–Mg alloys was studied, but in organic electrolytes [21]. The formation of Li_2MgSi was observed under these conditions. Similar behavior might be expected in a molten-salt environment.

3.3. Al anodes

A limited amount of work has been reported for the Al/FeS_2 couple in tetrachloroaluminate-based electrolytes [22–26]. However, this couple is of only limited use due to the low rate capabilities and the temperature limitations imposed by the nature of the electrolyte. Above 200 °C, the vapor pressure of $AlCl_3$ becomes appreciable. The use of Al anodes also results in a lower cell emf. Limited testing at SNL showed that an Al/$NaAlCl_4$/FeS_2 cell with a flooded anode (25 w/o electrolyte) yielded only 44 A-s g^{-1} to a 0.3-V cutoff when discharged at 250 °C at 16 mA cm^{-2} [27]. The cell showed extreme polarization—an order of magnitude greater than a Li(Si)/LiCl–KCl/FeS_2 cell when discharged at 400–500 °C. This caused the voltage to drop rapidly from an initial value of 1.05 V. The high cell impedance was most likely due to a high-resistance oxide film on the Al.

Some work has been reported in the literature for cells made using $AlCl_3$–NaCl electrolytes with Al anodes and $CuCl_2$ cathodes [28]. An open-circuit voltage of 1.77 V was reported. The same research group also examined $MoCl_5$ cathodes with Al anodes in the tetrachloroaluminate electrolyte. In related work, the Al anodes were replaced by LiAl anodes with the same cathodes [29–31]. However, those data are not representative, as the high activity of the LiAl anode would reduce the Al^{+3} species in the tetrachloroaluminate to Al metal, as shown in

$$AlCl_4^- + LiAl \rightarrow Al^0 + 4Cl^- + 3Li^+ \quad (4)$$

While systems based on tetrachloroaluminate electrolytes have been shown to be rechargeable, they are not practical for typical thermal-battery applications.

3.4. Pure Li anodes

The highest emf one can realize with thermal batteries would be to use pure Li as an anode material. However, since Li melts at only 180 °C, it would be liquid at thermal-battery operating temperatures and would have to be contained during battery operation. One way of accomplishing this is to use a metal foam or felt wick (e.g., Feltmetal®) to hold the molten Li is held in place by capillary action [32–35]. An alternative approach developed at CRC was to use a high-surface-area Fe powder to act as a binder, the so-called liquid anode or "LAN" [36]. This requires a large amount of material (~80 w/o), which greatly reduces the potential specific energy and energy density of the anode. In addition, it was necessary to use backing screens and a cup to fabricate the LAN so as to be suitable for use in thermal batteries under conditions of shock, vibration, or spin.

Szczesniak et al. compared the performance of the LAN with Li–Si (40 w/o Li), and Li–Al (20 w/o Li) anodes in LiCl–KCl eutectic electrolyte at 447 °C using half-cells with a Mo counter electrode [37]. As expected, compared to the Li–Si and Li–Al anodes, the LAN anodes had the highest potential, lowest impedance, and highest current efficiency but it had lower specific energy due to the large amount of Fe present.

Only limited performance data in actual cells have been reported in the literature. Miles used the LAN in a molten-nitrate electrolyte [38] but detailed electrochemical results for the LAN in full-sized thermal batteries are limited.

One of the main concerns with the use of molten Li as an anode in thermal batteries is the tendency for a displacement reaction to occur during discharge in the presence of K^+ in the electrolyte:

$$Li^0_{(liq)} + K^+ \rightarrow Li^+ + K_{(melt)} \quad (5)$$

This lowers the overall coulombic efficiency, as the *K* in the melt can escape and react with any surrounding oxide materials, such as insulation. Under a severe environment, there is the possibility of the escape of molten Li from the retaining cup, which can lead to shorting of cells. For these reasons, researchers turned to Li alloys for potential thermal-battery anodes. (A comprehensive review of the thermodynamic properties of Li binary alloys was published by Smith and Moser [39].)

3.5. Li–Al binary anodes

The bulk of the initial work with the sulfide-based systems (e.g., FeS_2) was with a Li–Al alloy containing 20 w/o Li, essentially LiAl in composition. This became the primary anode for all thermal batteries at both CRC [13] and KDI Score (later to become SAFT America) [40]. Several patents have been issued dealing with the preparation of Li–Al anodes [41,42]. Moshtev et al. reported on the performance in ambient-temperature batteries of Li–Al anodes made by a compression method [43]. Performance has also been reported for electrochemically formed Li–Al anodes [44].

Several patents describe preparation of Li–Al alloys for use in high-temperature batteries [45–47].

3.5.1. Phases

The phases that exist in the Li–Al system were examined during anode studies at room temperature in organic-based electrolytes [48]. Phases that were identified included Li, α-Al (solid solution), Li_9Al_4, Li_3Al_2 (γ), and β-LiAl. Similar work was conducted at ANL using molten salts such as the LiCl–KCl eutectic (m.p. = 352 °C) and the LiF–LiCl–LiBr eutectics (m.p. = 430 °C) [49]. The Li activity increased from 0.007 to ~0.7 over a composition range of 48–56 a/o

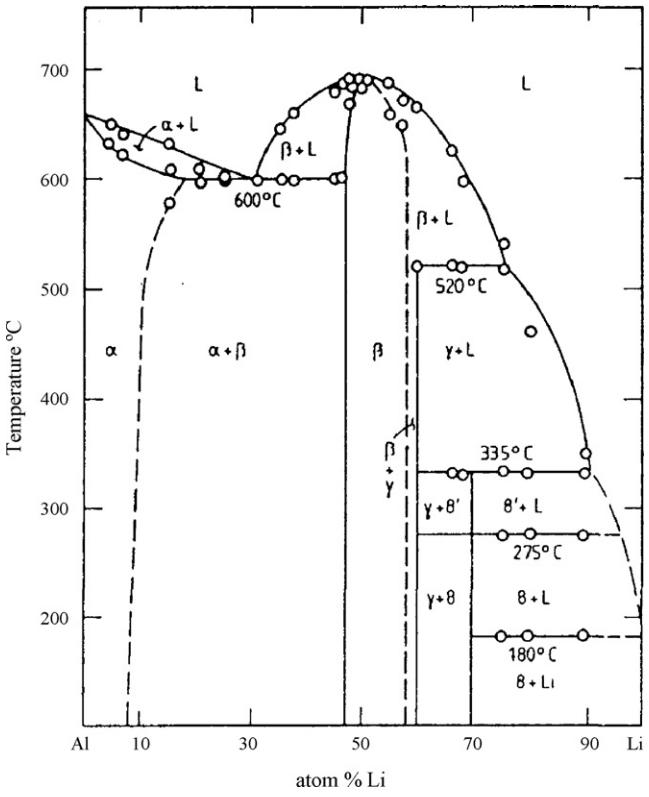

Fig. 4. Phase diagram for the Li–Al system.

Li (the β phase region). The compound Li_3Al_2 exits up to the peritectic decomposition temperature of 520 °C. (This material had previous been reported as Li_2Al.) The phase diagram for Li–Al is shown in Fig. 4 [50]. The free energies of formation for the γ phase was determined to be −58 kJ mol^{-1} while that for the β phase was −28.6 kJ mol^{-1}.

Subsequent work by Wen et al. studied the thermodynamic and mass-transport properties of the Li–Al system in LiCl–KCl eutectic electrolyte over a temperature range of 415–600 °C [51]. They reported the free energy of formation of the β phase to be −29.1 kJ mol^{-1} with the Li activity increasing from 0.0063 to 0.31 as the Li concentration increased from 46.8 to 55.0 a/o. At 423 °C, the γ phase was stable between 60.3 and 61.7 a/o L and the solid solubility of Li in Al (the α phase) was 9.2 a/o. At this temperature, the homogeneity range of the β phase was 46.8–56 a/o. The Li^+ diffusivity in β-LiAl was very composition dependent, changing from 1.6×10^{-6} to 0.30×10^{-6} cm^2 s^{-1} as δ changed from −0.1 to −0.17 in $Li_{1+\delta}Al$. The potential of the α + β region was found to be 297 mV vs. Li at 423 °C.

Based on these works, only the β-LiAl would be suitable for use as an anode in high-temperature batteries. The geometric (dimensional) stability of the anode is ensured by the β-LiAl phase (m.p. = 700 °C) when the battery temperature is the highest at the beginning of discharge (little Li consumed).

3.5.2. Discharge reactions

The discharge sequence in molten salts for the Li–Al anode containing 20 w/o Li involves the solid solution with Al and the LiAl phase. Thus, only a single anode transition is possible: LiAl (β) to Al (α). The discharge reaction for nonstoichiometric LiAl is shown in

$$Li_{0.47}Al_{0.53} \rightarrow Li_{0.0578}Al_{0.53} + 0.411Li^+ + 0.411e^- \quad (6)$$

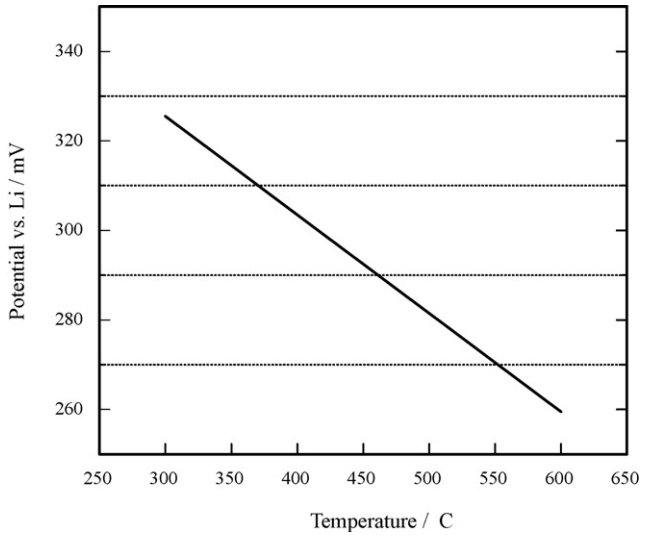

Fig. 5. Emf of LiAl alloy in the α + β mixed-phase region as a function of temperature.

This corresponds to a capacity of 2259 A-s g^{-1} for the two-phase, α + β discharge region. The emf for this region is plotted as a function of temperature in Fig. 5 [52].

The discharge of FeS_2 cathodes in LiCl–KCl eutectic electrolyte at 500 °C at 50 mA cm^{-2} with Mg and Li–Al–Mg anodes are compared in Fig. 6; comparable data for a Ca/$CaCrO_4$ cell are also included [53]. The Ca/$CaCrO_4$ cell has an initially higher voltage but a much lower capacity relative to the other cells. The voltage of the Mg/FeS_2 cell was much lower than that of the Li–Al–Mg/FeS_2 cell.

3.5.3. Related studies

The defect and disorder of the LiAl anodes have been studied by ANL [54]. These have an impact on the conduction mechanism. Neutron-diffraction results showed that there is disorder in β-LiAl at battery-operating temperatures and that the Al atoms are mobile. There is no phase change in β-LiAl on heating from room temperature to close to the melting point. The study showed that the specific

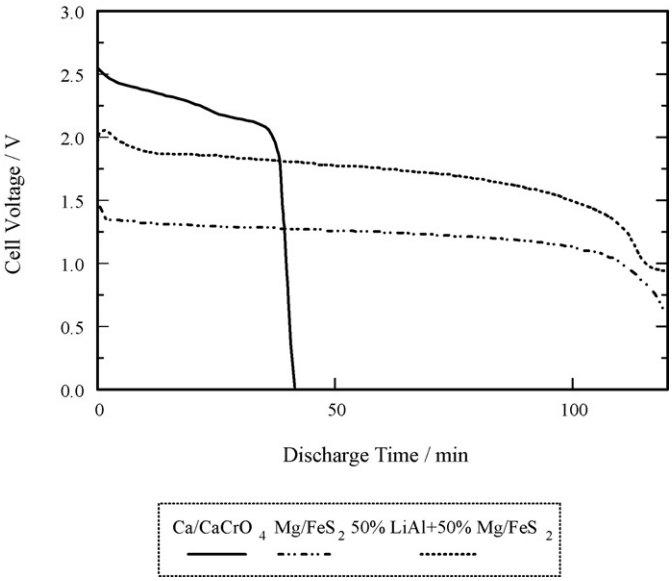

Fig. 6. Comparison of the discharge of Mg/FeS_2 (50% LiAl + 50% Mg)/FeS_2, and Ca/$CaCrO_4$ cells at 500 °C and 50 mA cm^{-2}.

energies of the Li–Al–Si electrodes were greater than those of the LiAl anode but less than those of the Li–Si anodes.

Borger et al. studied the relaxation processes in LiAl/FeS cells in LiCl–KCl and LiF–LiCl–LiF melts and found that the capacity-limiting process at high current densities was the Li transport through the α phase layer to the particle surface [55].It is claimed in a patent that the addition of graphite, Raney Ni, or Fe to the powdered LiAl anode was beneficial to electrode performance in molten-salt, high-temperature cells, but no detailed performance data were provided [56].

3.6. Li–Al ternary anodes

ANL initially studied the use of binary Li–Al anodes for possible use in high-temperature rechargeable batteries [49]. The work was extended to examine Li–Al–Si ternary compositions, with the intent of improving the specific energies [57]. The results showed that the specific energies of the ternary compositions were higher than the LiAl anode but less than those of the Li–Si anodes.

Ternary Li–Al–Fe anodes have been reported to outperform LiAl anodes by increasing the cell emf by ~200 mV [58]. They can be prepared by charging Li into Al_5Fe_2 alloys or by contact of the alloy with molten Li.

3.7. Li–Si binary anodes

3.7.1. Phases

The Li–Si phase diagram has been studied by numerous investigators in the past, but there have been discrepancies in the compositions of the phases reported. The earliest reported work was by Böhm [59]. He reported the phases Li_4Si ($Li_{15}Si_4$) and Li_2Si. Schaefer et al. studied a phase purported to be Li_7Si_2 in their work on the Li–Si phase diagram [60]. They also reported the existence of Li_4Si and Li_2Si [61,62]. Lai studied the Li–Si phase diagram by electrochemical titration in molten LiCl–KCl eutectic electrolyte and reported the phases Li_5Si, $Li_{22}Si_5$, $Li_{4.1}Si$, Li_4Si, $Li_{15}Si_4$, $Li_{2.8}Si$, and Li_2Si [63]. Sharma and Seefurth also examined the electrochemistry of the Li–Si system in LiCl–KCl and LiCl–LiBr–LiF electrolytes and reported the phases Li_2Si, $Li_{21}Si_8$, $Li_{15}Si_4$, and $Li_{22}Si_5$ [64]. In later work, they reported that Li diffusion in Si was greater than in Al (3.0×10^{-8} cm^{-2} s^{-1} vs. 1.2–1.7 $\times 10^{-10}$ cm^{-1} s^{-1}), which was the basis for a comprehensive study of current efficiencies of various Li–Si alloys at a number of current densities in these electrolytes [65]. Subsequently, von Schnering et al. performed detailed X-ray diffraction and electrochemical measurements on the purple "Li_2Si" phase and found it to actually be $Li_{14}Si_6$ or $Li_{2.33}Si$ [66].

It was the work of Wen and Huggins that finally eliminated the confusion as to the actual compositions of the equilibrium various phases that exist at high temperatures in the Li–Si system [67]. Through careful coulometric titrations in LiCl–KCl eutectic electrolyte, they were able to demonstrate that the stable intermediate phases are $Li_{12}Si_7$, Li_7Si_3, $Li_{13}Si_4$, and $Li_{22}Si_5$. Later work using differential scanning calorimetry was able to substantiate these results and provide additional data as to melting points and liquidus regions [68]. In addition, work at SNL corroborated these data [69]. The most recent phase diagram is presented in Fig. 7.[1]

3.7.2. Discharge reactions

A Li–Si anode was developed in the 1980s at SNL to replace the Li–Al one [53]. This anode had a number of advantages over the Li–Al counterpart, such as better rate capabilities and multiple phases.

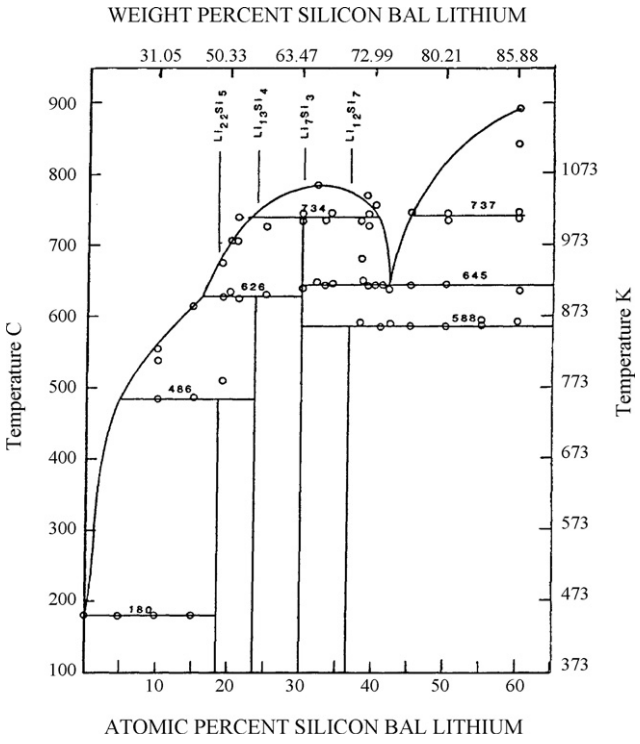

Fig. 7. Phase diagram of Li–Si system.

There are a number of compounds that form within the Li–Si system, with the emf vs. Li decreasing with higher Li contents. The discharge sequence for the Li–Si alloy anodes is shown in Eq. (7) and is based on the work of Wen and Huggins [67]:

$$Li_{22}Si_5(Li_{4.4}Si) \rightarrow Li_{13}Si_4(Li_{3.25}Si) \rightarrow Li_7Si_3(Li_{2.33}Si) \rightarrow Li_{12}Si_7(Li_{1.71}Si) \quad (7)$$

The preference was to use the $Li_{13}Si_4 \rightarrow Li_7Si_3$ transition (44 w/o Li) for most applications, as the $Li_{22}Si_5$ composition is reactive to moisture even under dry-room conditions of <3% relative humidity. The discharge reaction for this transition is shown in Eq. (8) and corresponds to a capacity of 1747 A-s g^{-1} of alloy:

$$Li_{13}Si_4 \rightarrow 4/3Li_7Si_3 + 11/3Li^+ + 11/3e^- \quad (8)$$

This is 29.3% lower than the capacity of the Li–Al anode material (Eq. (6)) on a weight basis. On a volume basis, the Li–Al anode capacity of 3931 A-s cm^{-3} is much greater than that for the Li–Si transition (Eq. (8)) of 2411 A-s cm^{-3}, due to the higher density of the Li–Al (1.74 g cm^{-3}) vs. the Li–Si (1.38 g cm^{-3}). However, the alloy has the capability of multiple transitions and can generally deliver power at a higher rate. The Li–Si alloy also tended to give more reproducible performance from batch to batch of material. It ultimately replaced the Li–Al anode in most thermal batteries.

The emfs vs. Li of the Li–Si system and Li–Al system in LiCl–KCl eutectic electrolyte as a function of Li content in the alloys are shown in Fig. 8 for temperatures of 415 and 427 °C, respectively [52,67]. The lower voltages vs. Li for the $Li_{13}Si_4$ anode make it the preferred choice for use in thermal batteries.

The most common cathode used with the Li–alloy anodes is pyrite. It can undergo a number of voltage transitions, as seen in Fig. 9 for a temperature of 415 °C [70]. The open-circuit cell voltages for the β-LiAl/FeS_2 and $Li_{13}Si_4$/FeS_2 cells are compared in Fig. 10 as a function of temperature with the LiCl–KCl eutectic electrolyte.

[1] The phases that form in ambient temperature applications are not always the same as those in hightemperature batteries [70,71].

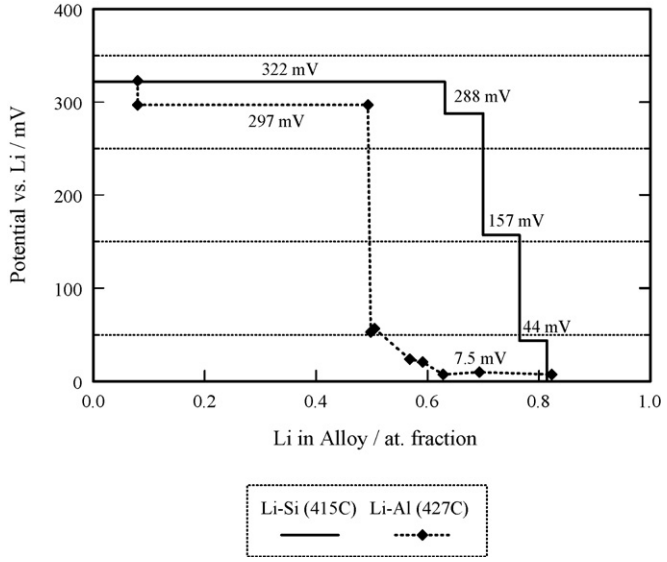

Fig. 8. Emfs of Li–Al and Li–Si alloys as a function of Li content.

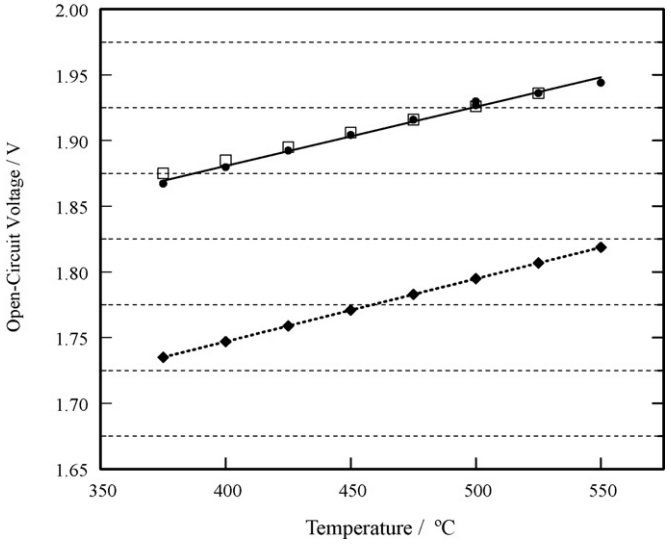

Fig. 10. Emfs of cells with FeS_2 cathodes and β-LiAl anodes (solid diamonds) and $Li_{13}Si_4$ anodes (solid circles) (measured at SNL). Open squares are values calculated from measured data for β-LiAl/FeS_2 cells and β-LiAl/Li couples.

The measured values for the Li–Si/FeS_2 cells are in good agreement with those calculated for the β-LiAl/FeS_2 couple and the β-LiAl–Li emfs.

3.7.3. Other electrochemical and transport properties

3.7.3.1. Power characteristics. The power capabilities of Li–Si anodes were studied by ANL for their rechargeable system. Typical data for several compositions are listed in Table 1 as a function of current density at a temperature of 460 °C; the electrolyte composition was not specified [71]. The lower phases (with less Li) did not have the power capabilities because of the lower rate of Li diffusion in the alloy under high-rate pulsing. These phases would not normally be encountered in normal thermal-battery operation.

3.7.4. Thermodynamic properties

Nikolaev et al. described the thermodynamic properties of Li–Si compounds reported in the literature using polarization measurements in various molten salts [72]. Table 2 summarizes the enthalpies and entropies of formation for a number of phases. The values for the various studies show reasonably good agreement.

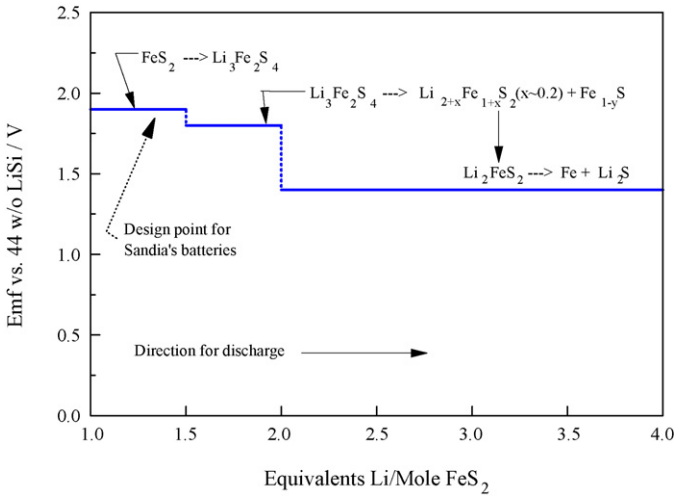

Fig. 9. Discharge sequence for FeS_2 cathodes in thermal batteries.

The partial molar enthalpy and entropy changes associated with the mixing of lithium for the two-phase regions of the Li–Si system are shown in Table 3.

3.7.5. Reactivity towards ambient gases

Li–Si alloys, like Li–Al ones, are sensitive towards reactive atmospheric gases such oxygen and water vapor. This is accelerated when the alloys are in a powdered form used in the manufacture of battery anode pellets. For that reason, it is necessary to process powders and pellets in a dry room environment where the relative humidity is typically <3%. (Solid Li foil is much less reactive to such gases as it is in an undivided state with much less surface area.) The initial oxygen content of a standard anode $Li_{13}Si_4$ powder is typically <0.5 w/o. However, during handling and pelletization, the final oxygen content can increase to >1.5 w/o. Excessive oxygen levels can result in increased fluidity of the electrolyte associated with the anode due to the presence of Li_2O, which acts as a wetting agent. This can lead to electrolyte leakage during discharge that can lead to parasitic shunting currents. While in theory, one could use the $Li_{22}Si_5$ composition to provide a higher cell voltage, the increased reactivity of this material makes it impractical to process. (It can generate significant heat during processing as a result of chemical reactions with oxygen and water vapor under dry-room conditions.) The reactivity of the Li alloys with nitrogen is generally not an issue under standard processing conditions.

Table 1
Power densities of Li–Si anodes at 46 °C as a function of composition [71]

Anode composition	Current density (mA cm^{-2})	Power (mW cm^{-2})
$Li_{2.85}Si$	607	316
	642	580
	922	866
	1230	738
Li_2Si	587	465
	894	626
	1230	692
	1580	463
$Li_{1.68}Si$	280	190
	600	349

Electrode thickness of 0.6 cm, unknown electrolyte.

Table 2
Enthalpies and entropies of formation of Li–Si compounds

Composition (a/o Li)	ΔH_f (kJ mol^{-1})				ΔS_f (J mol^{-1} K^{-1})	
	Ref. [66]	Ref. [56]	Ref. [55]	Ref. [66]	Ref. [56]	Ref. [55]
63.2	−26.6	−26.3	−26.3	−8.7	−8.8	−8.5
70.0	−28.3	−28.1	−27.3	−9.4	−9.6	−8.3
76.5	−28.8	−27.8	−27.2	−12.2	−11.2	−10.2
81.5	−26.1	−25.0	−24.2	−13.3	−11.9	−10.8

3.8. Li–Si ternary anodes

3.8.1. Li–Si–Fe alloys

A number of ternary Li–Si alloys have been proposed to improve the overall electrochemical performance. The Li–Si–Al system was described earlier in this paper. A Li–Si–Fe alloy was reported by Lai [73]. The ternary alloy was formed by charging Li into a ferrosilicon alloy, $FeSi_2$. The resulting alloy had a greater current efficiency relative to the corresponding binary formed by charging Li into Si. Similar results were reported for when $FeSi_2$ was replaced by $MgSi_2$. No alloys were prepared by direction combination of elements, so that these data are not necessarily relevant for thermal-battery use.

3.8.2. Li–Si–Mg alloys

Using existing phase-diagram and thermodynamic data, Anani and Huggins proposed the addition of select ternary elements to the Li–Si system to improve the performance [74]. One such element was Mg. The predicted emf at 415 °C of a system based on Mg_2Si–Mg–$Li_{13}Si_4$ was only 60 mV vs. Li, which compares to 157 mV for the standard $Li_{13}Si_4$–Li_7Si_3 anode (44 w/o). The predicted specific energy was also 34% greater [74,75]. The concept was demonstrated by charging Li into Mg_2Si and then discharging the ternary alloy. However, this expected improvement was not realized when the appropriate alloy composition was prepared by standard metallurgical techniques [27]. Additional annealing may be needed to ensure homogenous phase equilibria.

3.9. Li–Sb alloys

As seen in Fig. 11, there are a number of phases that exist in the Li–Sb system, such as Li_3Sb and LiSb [50]. The kinetics of the mass transfer of Li in Li_3Sb have been reported along with thermodynamic data [76]. The Li activity is 2.6×10^{-7} at 400 °C and the Li diffusion coefficient at 360 °C is 1.3×10^{-9} cm^2 s^{-1}. The emf of this compound is 800 mV vs. Li at 400 °C. This is much higher than the emf of 157 mV for the Li–Si anode with 44 w/o Li, which makes it much less attractive as a potential thermal-battery anode material (Fig. 12). In addition, there is the possibility of dissolution of Li_3Sb in the molten salts, which would increase the rate of self-discharge. This phenomenon has been reported for Na_3Sb, where that intermetallic behaved more like an ionized salt compound rather than an intermetallic due to the presence of antimonide (Sb^{-3}) [77].

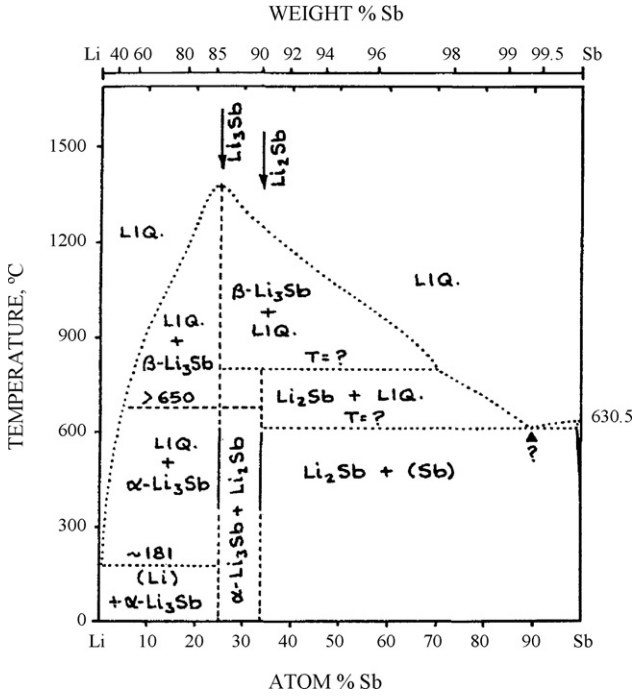

Fig. 11. Phase diagram of the Li–Sb system.

3.10. Li–Bi anodes

The thermodynamics of the Li–Bi system was studied using electrochemical titration in molten LiCl–LiF electrolyte [78]. The phases in the Li–Bi system (see Fig. 12) are similar to those on the Li–Sb system [50]. The emf of the Li_3Bi phase vs. Li is 720 mV at 487 °C, which is slightly lower than that of the Li_3Sb phase, but still too high to make it a candidate for use in thermal batteries. In addition, the low melting points for LiBi and, especially, Bi (271.3 °C) could lead to intercell shorting problems in a battery as Li is extracted from Li_3Bi during discharge.

3.11. Li–Sn alloys

3.11.1. Phases

As in the case of the Li–Si system, there have been a number of studies of the Li–Sn system by various researchers. However, there have been discrepancies among the various studies. The ear-

Table 3
Partial molar enthalpies and entropies of Li in the two-phase regions of the Li–Si system

Composition (a/o Li)	ΔH_{mix} (kJ mol^{-1})				ΔS_{mix} (kJ mol^{-1} K^{-1})	
	Ref. [72]	Ref. [64]	Ref. [63]	Ref. [72]	Ref. [64]	Ref. [63]
Li + $Li_{12}Si_7$	−42.13	−41.52	−42.56	−13.8	−13.9	−13.5
$Li_{12}Si_7$ + $Li_{14}Si_6$	−35.86	−36.30	−32.04	−12.3	−12.6	−7.44
$Li_{14}Si_6$ + $Li_{13}Si_4$	−30.64	−26.72	−26.68	−21.8	−16.9	−17.0
$Li_{13}Si_4$ + $L_{22}Si_5$	−16.05	−14.72	−13.29	−17.7	−14.7	−12.9

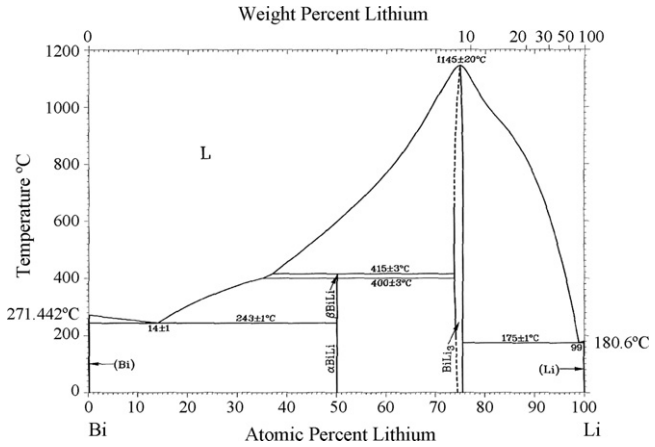

Fig. 12. Phase diagram of Li–Bi system.

liest work claimed Li_4Sn, Li_3Sn_2, and Li_2Sn_5 as the primary phases. Later work showed that the "Li_4Sn" phase was actually $Li_{22}Sn_5$. Subsequent X-ray diffraction studies confirmed the presence of LiSn, Li_5Sn_2, and Li_7Sn_2 and found two additional phases, Li_7Sn_3 and $Li_{13}Sn_5$. More recently Wen and Huggins reinvestigated the Li–Sn phase diagram by coulometric titration in molten LiCl–KCl eutectic electrolyte [79]. The phase diagram that resulted from this work is presented in Fig. 13.

3.11.2. Discharge reactions

The discharge sequence for the Li–Sn alloy anodes is shown in Eq. (9) [79]:

$$Li_{22}Sn_5(Li_{4.4}Sn) \rightarrow Li_7Sn_2(Li_{3.5}Sn) \rightarrow Li_{13}Sn_5(Li_{2.6}Sn) \rightarrow Li_5Sn_2(Li_{2.5}Sn) \rightarrow Li_7Sn_3(Li_{2.33}Sn) \rightarrow LiSn \quad (9)$$

The emf vs. Li for the Li–Sn system is presented in Fig. 14 as a function of composition. Only the Li_7Sn_3 + LiSn region has any significant capacity of the various discharge possibilities for thermal-battery applications. However, the emf of this region is 450 mV vs. Li at 415 °C, which is much higher than the value of 157 mV for the $Li_{13}Si_4 + Li_7Si_3$ region. The discharge of the Li_7Sn_3 phase to LiSn is shown in

$$Li_7Sn_3 \rightarrow 3LiSn + 4e^- + 4Li^+ \quad (10)$$

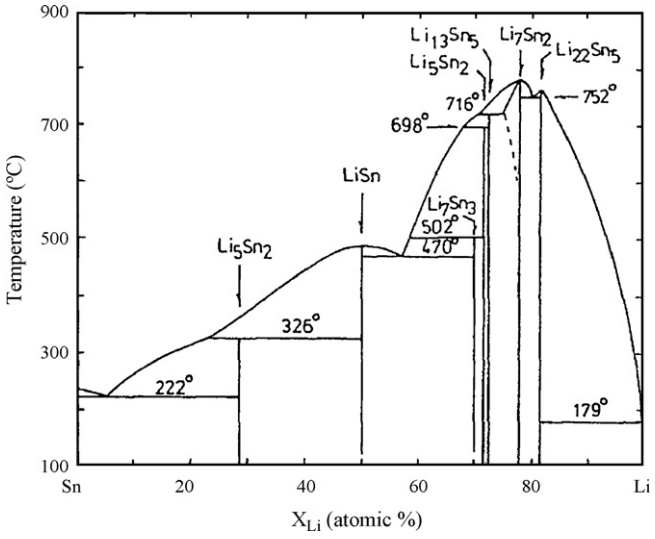

Fig. 13. Phase diagram of Li–Sn system.

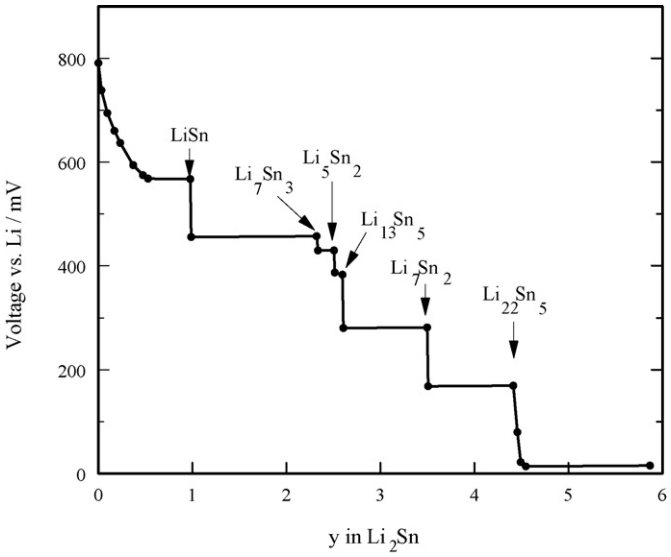

Fig. 14. Emfs of Li–Sn alloys at 415 °C as a function of Li content.

The capacity for this transition is 954 A-s g^{-1} of alloy, which is only about half that for the Li–Si counterpart (Eq. (8)). The low relative capacity coupled with the low melting point of the discharge phases could lead to intercell shorting in a thermal battery. As a result, it is of little use for such applications.

3.11.3. Thermodynamic properties

The thermodynamic properties of Li–Sn alloys at 415 °C were reported by Wen and Huggins as part of their comprehensive study of the Li–Sn system [79]. The activity of Li–Sn alloys was reported by Barsoum and Tuller over a temperature range of 320–380 °C [80]. The enthalpies of mixing of Li–Sn alloys were measured by Moser et al. from 418 to 665 °C [81]. A maximum value of −40 kJ mol^{-1} was determined near an alloy composition of Li_4Sn.

3.12. Mixed-conductor anodes

Boukamp et al. have proposed a somewhat different approach for the development of improved anodes for high-temperature applications [82]. It involves the dispersion of an anode such a Li–Si or Li–Al in a dense, solid, mixed-conductor matrix. This type of electrode would replace the typical porous one filled with salt. The matrix must have good electronic conductivity with a high diffusion coefficient for Li. It must not react with the dispersed anode phase and only provides a means of rapid mass transport of Li to the anode–separator interface. In their work, the $Li_{13}Sn_5$ phase was used as the matrix with $Li_{12}Si_7$ as the reactant phase, which was formed by charging Li into Si metal. This approach was also studied with Li–Cd reactant alloy phases [83,84]. While this approach may have merit for rechargeable systems, it is not practical for typical thermal-battery applications.

3.13. Li–B binary anodes

The Li–B system contains a number of compounds but all of the structures have not been characterized completely [85,86]. Li–B alloys have been examined for use as anodes in thermal batteries. Preparation of the alloy is complicated and involves a four-step heating process to obtain a homogenous material due to the exothermic nature of the reactions [87]. The actual anode actually consists of a porous, solid, lithium-boride matrix filled with

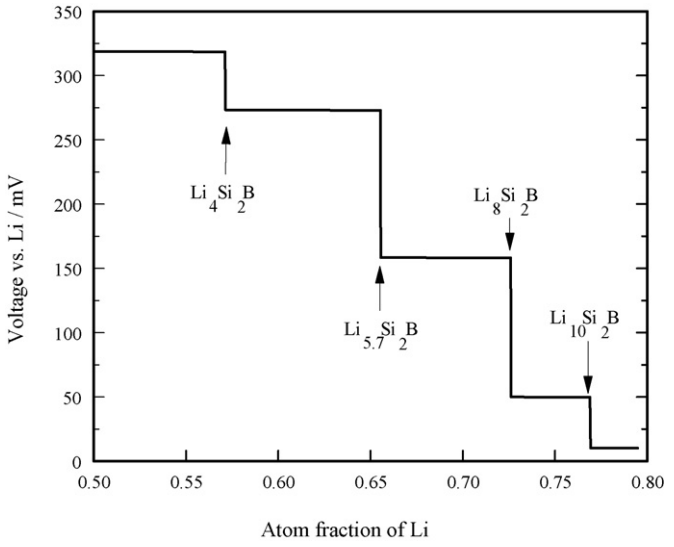

Fig. 15. Emfs of Li–Si–B alloys at 40 °C as a function of Li content.

Li [88]. A number of intermediate Li–B phases form during the reaction [89].

The discharge characteristics of Li–B alloys have been studied in molten-nitrate electrolytes [90,91] as well as in LiCl–KCl eutectic electrolytes [92-95]. A $Li_{0.78}B_{0.22}$ anode also has been studied as an anode in Li/Cl_2 cells [96]. Because the active anode material is Li, it has a very high rate capability (>8 A cm^{-2}) in LiCl–KCl eutectic at 600 °C [93]. Devries et al. found the solid matrix phase to be Li_2B [95]. Starting with an alloy composition of 70 w/o (78.4 a/o) Li, a discharge capacity of 4800 A-s g^{-1} of alloy was obtained, which increased to 7700 A-s g^{-1} for 80 w/o (86.2 a/o) Li [93]. This is many times higher than what can be realized with Li–Al or Li–Si anodes (Eqs. (6) and (8), respectively).

There was considerable interest in adapting Li–B alloys to replace the anode in Li–Si/FeS_2 thermal batteries. It has the advantage of performing as a pure-Li anode, being only 20 mV more positive than Li, and remaining solid at thermal-battery operating temperatures. Difficulty in scaling from small, sized laboratory-sized batches to larger, commercial scale prevented its use in thermal batteries [95]. The inherent variability in composition from batch to batch lead to unacceptable variability in performance, which would not be acceptable for conventional thermal batteries.

3.14. Li–B ternary anodes

3.14.1. Li–Si–B alloys

The advantages of the Li–Si and Li–B systems were incorporated in the development of Li–Si–B ternary alloys [97–99]. It was also felt that the reduced activity of Li in the alloy relative to pure Li would reduce the tendency for the formation of K vapors by a displacement reaction with K^+. An alloy of initial composition $Li_{10}Si_2B$ was discharged at 400 °C in LiCl–KCl eutectic using a half-cell with an Al counter electrode. There are multiple voltage transitions for the alloy as the composition changes during discharge, as shown in Fig. 15 The $Li_{10}Si_2B \rightarrow Li_8Si_2B$ transition has a potential that is 50 mV vs. Li, which is much less than that of 157 mV for the $Li_{13}Si_4 \rightarrow Li_7Si_3$ transition (Eq. (8)). The first voltage transition is given by

$$Li_{10}Si_2B \rightarrow Li_8Si_2B + 2Li^+ + 2e^- \quad (11)$$

The capacity for Eq. (11) is 1415 A-s g^{-1}, which is less than capacity 1747 A-s g^{-1} for $Li_{13}Si_4$ for the first voltage transition. The second voltage transition is shown in

$$Li_8Si_2B \rightarrow Li_{5.7}Si_2B + 2.3Li^+ + 2.3e^- \quad (12)$$

The capacity for this transition is 1811 A-s g^{-1} and its emf is the same as that for the standard Li–Si discharge transition (Eq. (8)). Thus, the Li_8Si_2B anode would provide slightly more capacity.

However, if one can use the capacity of the two transitions, i.e., for $Li_{10}Si_2B$ to $Li_{5.7}Si_2B$, then the overall capacity can be increased to 3226 A-s g^{-1}, which would be a considerable improvement over the standard Li–Si alloy with 44 w/o Li. Similarly, if one can use the $Li_{22}Si_5 \rightarrow Li_{13}Si_4$ transition as well for the Li–Si alloy (i.e., for $Li_{22}Si_5 \rightarrow Li_7Si_3$), the overall capacity would increase to 3402 A-s g^{-1}, which is somewhat higher than for the Li–Si–B transitions. However, the high reactivity of the $Li_{22}Si_5$ compound with ambient oxygen and moisture even under dry-room conditions precludes its use. If the $Li_{10}Si_2B$ phase is not as reactive as the $Li_{22}Si_5$ phase, then a two-transition discharge may be feasible. However, where tight voltage regulations are imperative for some thermal-battery applications, the loss of ~100 mV per cell during the second phase transition ($Li_8Si_2B \rightarrow Li_{5.7}Si_2B$) would not be acceptable. The deciding factor between the Li–Si and Li–Si–B alloys could be the relative costs. B is much more expensive than Si, so that the addition of B may not provide any intrinsic advantages over the standard Li–Si anode with 44 w/o Li. Without density data for the Li–Si–B alloys, one cannot calculate the energy densities of these materials for comparison to the Li–Si compounds.

3.14.2. Li–Mg–B alloys

The use of Mg as an addition to Li–B alloys to produce ternary alloys has been reported but no electrochemical tests were conducted [100].

3.15. Li–Ge anodes

Grigor'eva et al. studied the electrochemical behavior of Li_4Ge and Li_3Ge using half-cells with an Al counter electrode in LiCl–KCl eutectic electrolyte at 650 and 750 °C [101]. The compositions were reported to be stable phases in the Li–Ge system [102] and were prepared by melting Li and Ge together in the appropriate amounts. They postulated the appearance of $Li_{15}Ge_4$ and Li_2Ge along with an unidentified phase during the charge/discharge studies.

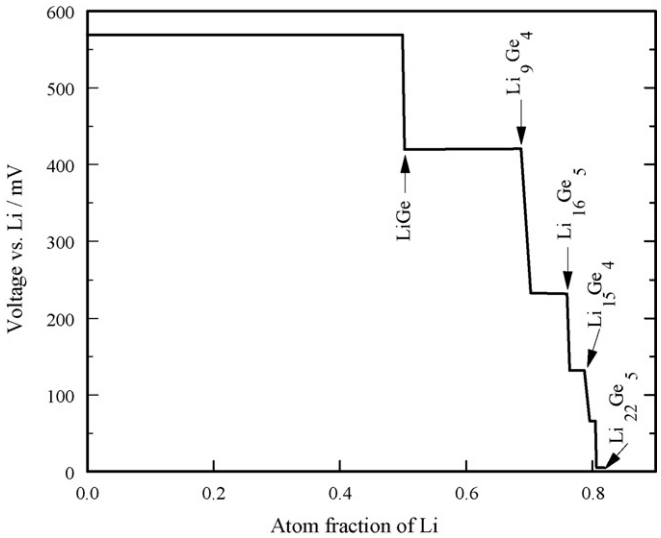

Fig. 16. Emfs of Li–Ge alloys at 40 °C as a function of Li content.

Table 4
Capacities and plateau voltages for candidate Li-alloy anodes

Anode	Capacity (A-s g^{-1})	Capacity (A-s cm^{-3})	Discharge emf/mV vs. Li^0 (T/°C)
Li in LAN (20 w/o Li)	2781	5808	0
Li in Ni wick (17% dense)	3019	5896	0
Li–Al (20 w/o Li)	2259	3931	297 (415)
$Li_{13}Si_4$ (44 w/o Li) (1st transition)	1747	2411	157 (415)
Mg_2–Mg–$Li_{13}Si_4$	3155	>4354	60 (415)
Li–B (70 w/o Li)	4800	3900	20 (500)
Li–B (80 w/o Li)	7700	5400	20 (500)
$Li_{10}Si_2B$ (50.9 w/o Li) (1st transition)	1415	–[a]	50 (400)
Li_8Si_2B (45.3 w/o Li) (1st transition)	1811	2880	157 (400)
Li_7Sn_3 (12 w/o Li) (1st transition)	954	–[a]	450 (415)
Li_9Ge_4 (17.7 w/o Li) (1st transition)	1368	3420 (est.)	420 (400)
$Li_{16}Ge_5$ (23.4 w/o Li) (1st transition)	967	2418 (est.)	236 (400)

[a] Density value needed for calculation not available.

Nikolaev and Demidov galvanostatically charged Li into a pressed-Ge electrode in molten LiCl–KCl–LiF eutectic and a LiCl–LiBr–LiF electrolyte at 450 °C [103]. According to their results, they determined that the intermetallic phases stable under these conditions were LiGe, Li_2Ge, Li_9Ge_4, Li_3Ge, $Li_{15}Ge_4$, and $Li_{22}Ge_5$. The latter compound has been reported to be the stable phase at high Li activity [104].

Sammells et al. also examined the Li–Ge system in a similar manner at 400 °C using a Ge electrode and a β-LiAl reference and counter electrode in LiCl–KCl eutectic [105,106]. The composition–emf diagram that was constructed from the work is shown in Fig. 16. There were a number of voltage plateaus formed due to the various phase transitions. The only one appropriate for thermal-battery use is the Li_9Ge_4–LiGe region. The discharge reaction for this is shown in

$$Li_9Ge_4 \rightarrow 4LiGe + 5Li^+ + 5e^- \quad (13)$$

This corresponds to a discharge capacity of 1368 A-s g^{-1}, which is much less than that for the standard Li–Si alloy anode with 44 w/o Li (Eq. (8)). However, this Li–Ge discharge region has a potential of 420 mV vs. Li, which makes it unattractive. The next plateau with a lower emf is the $Li_{16}Ge_5$–:Li_9Ge_4 transition, with an emf of 236 mV, which is much higher than that for Eq. (8) of 157 mV. The capacity for this region is only 967 A-s g^{-1}. In addition to the higher emfs for the Li–Ge alloys, they suffer from the very high cost of Ge metal. Consequently, they do not appear promising as potential anode materials for thermal batteries.

3.16. Comparison of anode materials

The capacities for the major alloy phases considered as potential thermal-battery anodes are summarized in Table 4 along with the corresponding plateau voltages. The Li–B alloys have the highest specific energies with emfs close to pure Li, behaving, for all intents and purposes, as Li anodes. However, the corresponding energy densities are less than those of the pure-Li anodes, which are the highest of all the anodes. The difficulties associated with the production of Li–B alloys has limited their practical utilization as anodes. The Li–Mg–Si anode has a theoretical capacity greater than those of β-LiAl and the standard $Li_{13}Si_4$ anode, but this has not yet been realized in single-cell tests. While the capacity for the β-LiAl anode is higher than the first transition of the $Li_{13}Si_4$ anode, its emf is much more positive, reducing the overall voltage of a cell (e.g., with FeS_2 cathode). The limited work with the Li–Si–B alloys suggests that these are potential anode candidates. The Li_8Si_2B composition is attractive as it has an emf identical to that of $Li_{13}Si_4$ with a somewhat higher specific energy and energy density. The Li_9Ge_4 alloy has a reasonable specific energy and much higher energy density than $Li_{13}Si_4$. The Li_7Sn_3 phase has a low capacity and high emf vs. Li and would not be a practical alloy candidate.

4. Conclusions

The relevant chemical and electrochemical properties of a number of Li alloys have been described in terms of suitability for use as potential anodes in thermal batteries. The current preferred choice is the Li–Si alloy with 44 w/o Li ($Li_{13}Si_4$). It has a lower specific energy and energy density for the first transition (to form Li_7Si_3) than β–LiAl, which it has replaced in most applications, but provides ~150 mV greater voltage in a cell, which is important for high-voltage thermal batteries, as this reduces the number of cells required. However, it can undergo additional transitions, which results in greater battery life due to the built-in additional discharge capacity.

The LAN and Li-filled felts material provides the greatest possible cell voltage but the overhead associated with the high Fe content or matrix weights, respectively, reduces the ultimate capacity possible. The LAN has been successfully used in the past in thermal batteries. The Li–Mg–Si ternary alloy has attractive capacities but has never been successfully used in cells; more work with this material (including battery tests) is merited, because of the low plateau voltage of only 60 mV vs. Li. Another candidate worthy of additional research is Li_8Si_2B, which has an emf equal to that of $Li_{13}Si_4$ but with somewhat higher specific energy and energy density. This material should be tested in single cells and batteries to see if all of its potential can be realized. Li–Sn and Li–Bi alloys has low-melting phases that could interfere with thermal-battery operation due to possible cell shorting and not considered viable anode candidates. Li–Ge alloys have emfs that are too high vs. Li for thermal batteries and have the additional limitation of Ge being exorbitantly expensive.

References

[1] R.A. Guidotti, P. Masset, J. Power Sources 161 (2) (2006) 1443.
[2] P. Masset, R.A. Guidotti, J. Power Sources 164 (1) (2006) 397.
[3] P.J. Masset, R.A. Guidotti, J. Power Sources 177 (2) (2008) 456.
[4] P.J. Masset, R.A. Guidotti, J. Power Sources 178 (1) (2008) 595.
[5] H. Goldsmith, J.T. Smith, J. Electrochem. Soc. 6 (1–2) (1968) 16.
[6] H.A. Laitenen, J.W. Pankey, J. Am. Chem. Soc. 81 (1959) 1053.
[7] H.A. Laitenen, C.H. Liu, J. Am. Chem. Soc. 80 (5) (1957) 1015.
[8] D.A. Nissen, J. Electrochem. Soc. 126 (2) (1979) 176.
[9] R.A. Guidotti, F.W. Reinhardt, Anodic reactions in the Ca/$CaCrO_4$ thermal battery, Sandia National Laboratories report SAND83-2271, September, 1985, many SAND reports are available at http://www.osti.gov/bridge.
[10] S.K. Preto, L.E. Ross, N.C. Otto, J.F. Lomax, M.F. Roche, Proceedings of the 16th IECEC 1, 1981, p. 765.
[11] D.L. Barney, M.F. Roche, S.K. Preto, L.E. Ross, N.C. Otto, F.J. Martino, Calcium/Metal-Sulfide Battery Development Program Progress Report for October 1979–September 1980, Argonne National Laboratory report ANL-79-1, 1979.

[12] L.E. Ross, S.K. Preto, N.C. Otto, C.C. Sy, M.F. Roche, Proceeding of the 15th IECEC 1, 1980, p. p581.
[13] A.A. Schneider, S.E. Long, G.C. Bowser, Multishot thermal battery, final report AD0785584, Catalyst Research Corp., June, 1974 (Available from National Technical Information Service.).
[14] D.M. Bush, The Mg/FeS_2 system for thermal batteries, Sandia National Laboratories report SAND78-0084, July, 1978.
[15] High-performance batteries for electric-vehicle propulsion and stationary energy storage, Progress Report for October 1977–September 1978, Argonne National Laboratory report ANL-78-94, 1978.
[16] A. Isenberg, U.S. Patent 4,054,729 (October 18, 1977).
[17] M.-L. Saboungi, M. Blander, J. Electrochem. Soc. 122 (12) (1975) 1631.
[18] Y. Iwadate, M. Lassouani, F. Lantelme, M. Chemla, J. Appl. Electrochem. 17 (1987) 385.
[19] M. Sahoo, J.T.N. Atkinson, J. Mater. Sci. 17 (1982) 3564.
[20] W. Gasior, Z. Moser, W. Zakulski, G. Schwitzgebel, Metall. Mater. Trans. 27 (9) (1996) 1073.
[21] G.A. Roberts, E.J. Cairns, J.A. Reimer, J. Electrochem. Soc. 151 (4) (2004) A493.
[22] N. Takami, N. Koura, Proceedings of Stationary Energy Storage Load Leveling and Remote Applications, vol. 88-11, The Electrochemical Society, Princeton, NJ, 1988, p. 106.
[23] K. Koura, J. Electrochem. Soc. 127 (1980) 1529.
[24] K. Koura, Progress Batteries Sol. Cells 3 (1980) 260.
[25] N. Takami, N. Koura, Electrochim. Acta 33 (1) (1988) 69.
[26] N. Takami, N. Koura, Denki Kagaku 56 (1) (1988) 28.
[27] R.A. Guidotti, unpublished data.
[28] C.L. Hussey, J.K. Erbacher, L.A. King, Frank J. Seiler Research Laboratory Technical Report 76-0003, U.S. Air Force Academy, Colorado Springs, CO, 1976.
[29] J.K. Erbacher, C.L. Hussey, L.A. King, Proceedings of the 28th Power Sources Symposium, 1978, p. 84.
[30] D.M. Ryan, R.A. Marsh, R.K. Bunting, Proceedings of the 28th Power Sources Symposium, 1978, p. 90.
[31] R.A. March, D.M. Ryan, J.C. Nardi, J. Power Sources 3 (1978) 95.
[32] D.A. Vissers, B.S. Tani, U.S. Patent 3,933,521 (January 20, 1976).
[33] D.A. Vissers, Z. Tomczuk, R.K. Steunenberg, J. Electrochem. Soc. 121 (5) (1974) 665.
[34] G.C. Bowser, J.R. Moser, U.S. Patent 3,930,888 (January 6, 1976).
[35] G.C. Bowser, J.R. Moser, U.S. Patent 3,891,460 (June 24, 1975).
[36] D.E. Harney, U.S. Patent 4,221,849 (September 9, 1980).
[37] B. Szczesniak, Z. Burdka, S. Tabat, S. Stycznski, Proceedings of the Fourth Advanced Batteries and Accumulators International Conference (BRNO 2003), Brno University of Technolgoy, the Czech Republic, 2003.
[38] M.H. Miles, Proceedings of the 14th Annual Battery Conference on Applications and Advances, 1999, p. 39.
[39] J.F. Smith, Z. Moser, J. Nucl. Mater. 59 (1976) 158.
[40] P.V. Dand, K.K. Press, Improved thermal battery, final report ADA075835, KDI Score Inc., April, 1979.
[41] J.L. Settle, K.M. Myles, J.E. Battles, US Patent 3,957,532 (May 18, 1976).
[42] J.C. Schaefer, US Patent 3,981,743 (September 21, 1976).
[43] R.V. Moshtev, P. Zlatilova, B. Puresheva, V. Manev, A. Kozawa, J. Power Sources 51 (1994) 409.
[44] K.C. Gay, D.R. Vissers, F.J. Martino, K.E. Anderson, J. Electrochem. Soc. 123 (11) (1976) 1591.
[45] J.E. Battles, K.M. Myles, J.L. Settle, U.S. Patent 3,957,532 (May 18, 1976).
[46] J.E. Battles, T.W. Olszanski, Z. Tomczuk, U.S. Patent 4.011,372 (March 8, 1977).
[47] E.S. Buzzelli, U.S. Patent 3,607,413 (September 21, 1971).
[48] B.M.L. Rao, R.W. Francis, H.A. Christopher, J. Electrochem. Soc. 124 (10) (1977) 1490.
[49] J.R. Selman, D.K. DeNuccio, C.J. Sy, R.K. Steunenberg, J. Electrochem. Soc. 124 (8) (1977) 1160.
[50] Binary Alloy Phase Diagrams, 2nd ed., Vers. 1.0, ASM International, Materials Park, OH.
[51] C.J. Wen, B.A. Boukamp, R.A. Huggins, J. Electrochem. Soc. 126 (12) (1979) 2258.
[52] N.P. Yao, L.A. Herédy, R.C. Saunders, J. Electrochem. Soc. 118 (7) (1971) 1039.
[53] D.M. Bush, The Li/FeS_2 system for thermal batteries, Sandia National Laboratories report SAND77-0470, June, 1979.
[54] T.O. Brun, J.D. Jorgensen, M. Misawa, F.J. Rotella, S. Susman, J. Electrochem. Soc. 129 (11) (1982) 2509.
[55] W. Borger, W. Kappus, H.S. Panesar, Proceeding of the 17th IECEC, 1982, p. 544.
[56] T. Kaun, U.S. Patent 4,358,513 (November 9, 1982).
[57] L. Redey, D.R. S Vissers, Extended Abstracts of the Spring Meeting of The Electrochemical Society, vol. 84-2, The Electrochemical Society, Princeton, NJ, 1984, p. 175.
[58] T.D. Kaun, U.S. Patent 4,158,720 (June 19, 1979).
[59] H. Böhm, Z. Metallkunde 50 (1) (1959) 44.
[60] H. Schäfer, H. Axel, A. Weiss, Z. Naturforsch. 20 (1965) 1010.
[61] H. Schäfer, B. Eismann, W. Müller, Angew. Chem. Int. Edit. 12 (1973) 694.
[62] H. Schäfer, H. Axel, A. Weiss, Z. Naturforsch., B 20 (1965) 11302.
[63] S.-C. Lai, J. Electrochem. Soc. 123 (8) (1976) 1196.
[64] R.A. Sharma, F.N. Seefurth, J. Electrochem. Soc. 123 (12) (1976) 1763.
[65] R.A. Sharma, F.N. Seefurth, J. Electrochem. Soc. 124 (8) (1977) 1207.
[66] H.-G. von Schnering, R. Nesper, K.-F. Tebbe, J. Curda, Z. Metallkunde 71 (1980) 357.
[67] C.J. Wen, R.A. Huggins, J. Solid State Chem. 37 (1981) 271.
[68] C. van der Marel, G.J.B. Vinke, W. van der Lugt, Solid State Commun. 54 (11) (1985) 917.
[69] M.M. Karnowsky, J.D. Murray, The lithium–silicon phase diagram, Sandia National Laboratories report SAND84-0741J, 1984.
[70] Z. Tomczuk, D.R. Visser, J. Electrochem. Soc. 133 (12) (1986) 2505.
[71] D.R. Vissers, L. Redey, Electrochemical characteristics of lithium–silicon alloys electrodes for high-temperature-battery applications, Argonne National Laboratory report CONF-83-0999-01, 1983.
[72] V.P. Nikolaev, A.G. Morachevskii, A.I. Demidov, E.V. Bairachnyi, Zh. Prikl. Khim. 53 (9) (1980) 2088.
[73] S.-C. Lai, U.S. Patent 4,048,395 (September 13, 1977).
[74] A. Anani, R.A. Huggins, J. Power Sources 38 (1992) 351.
[75] A. Anani, R.A. Huggins, U.S. Patent 4,950,566 (August 21, 1990).
[76] W. Weppner, R.A. Huggins, J. Electrochem. Soc. 124 (10) (1977) 1569.
[77] M. Okada, R.A. Guidotti, J.D. Corbett, Inorg. Chem. 7 (1968) 2118.
[78] M.S. Foster, S.E. Wood, C.E. Crouthamel, Inorg. Chem. 3 (1964) 1428.
[79] C.J. Wen, A. Huggins, J. Electrochem. Soc. 128 (6) (1981) 1181.
[80] M.W. Barsoum, H.L. Tuller, Metall. Trans. 19A (1988) 637.
[81] Z. Moser, W. Gasior, F. Sommer, G. Schwitzgebel, J. Predel, Metall. Trans. 17B (4) (1986) 791.
[82] B.A. Boukamp, G.C. Lesh, R.A. Huggins, J. Electrochem. Soc. 128 (4) (1981) 725.
[83] A.A. Anani, S. Crouch-Baker, R.A. Huggins, J. Electrochem. Soc. 135 (8) (1988) 2103.
[84] A.A. Anani, S. Crouch-Baker, R.A. Huggins, in: A.N. Day (Ed.), Proceedings of the Symposium on Lithium Batteries, vol. 87-1, The Electrochemical Society, Princeton, NJ, 1987, p. 382.
[85] G. Mair, R. Nesper, H.G. von Schnering, J. Solid State Chem. 75 (1) (1988) 30.
[86] H. Rosner, W.E. Pickett, Phys. Rev. B 67 (2003) 054104.
[87] F.E. Wang, U.S. Patent 4,110,111 (September 29, 1978).
[88] Z. Liu, Z. Li, W. Duan, X. Qu, B. Huang, S. Zhang, Mater. Sci. Technol. 16 (6) (2000) 581.
[89] Z. Liu, X. Qu, Z. Li, B. Huang, Sci. China (Ser. E) 46 (4) (2003) 391.
[90] G.E. McManis, A.N. Fletcher, M.H. Miles, U.S. Patent 4,535,037 (August 13, 1985).
[91] G.E. McManis, M.H. Miles, A.N. Fletcher, J. Electrochem. Soc. 131 (2) (1984) 283.
[92] P. Sanchez, C. Belin, G. Crepy, A.de. Guibert, J. Mater. Sci. 27 (1) (1992) 240.
[93] S.D. James, L.E. Devries, J. Electrochem. Soc. 123 (3) (1976) 321.
[94] L.E. Devries, L.D. Jackson, J. Electrochem. Soc. 126 (6) (1979) 993.
[95] R.A. Sutula, F.E. Wang, U.S. Patent 4,162,352 (July 24, 1979).
[96] R. Szwarc, S. Dallek, Li(B) ingot preparation scale-up study. Final report, General Electric Neutron Devices report GEPP-TM-645, 1982 (OSTI ID: 5272805; DE82015798).
[97] A.F. Sammells, J. Electrochem. Soc. 125 (10) (1978) 1632.
[98] A.F. Sammells, U.S. Patent 4,116,780 (September 26, 1978).
[99] A.F. Sammells, U.S. Patent 4,076,905 (February 28, 1978).
[100] R.A. Sutula F.E. Wang, U.S. Patent 5,156,806 (May 5, 1975).
[101] E.M. Grigor'eva, M.A. Volgin, A.L. A'vov, Sov. Electrochem. 18 (11) (1982) 1311.
[102] S.P. Alisova, P.B. Budberg, in: N.V. Ageev (Ed.), Germanium–Lithium. Phase Diagrams of Metallic Systems (in Russian), vol. 12, VINITI, Moscow, 1968, p. 62.
[103] V.P. Nikolaev, A.L. Demidov, Sov. Electrochem. 19 (1983) 751.
[104] A.T. Dadd, P. Hubberstey, J. Chem. Soc., Faraday Trans. 1 (77) (1981) 1865.
[105] A.F. Sammells, M.R. St. John, U.S. Patent 4,346,152 (August 24, 1972).
[106] St.M.R. John, A.J. Furgala, A.F. Sammells, J. Electrochem. Soc. 129 (2) (1982) 246.